Multi-phase volcanic resurfacing at Io's Loki Patera

K. de Kleer*[a], M. Skrutskie[b], J. Leisenring[c], A.G. Davies[d], A. Conrad[e], I. de Pater[a], A. Resnick[f], V. Bailey[g], D. Defrère[h], P. Hinz[c], A. Skemer[i], E. Spalding[c], A. Vaz[c], C. Veillet[e], C.E. Woodward[j]

[a]*Department of Astronomy, University of California, Berkeley*
[b]*Department of Astronomy, University of Virginia*
[c]*Steward Observatory, University of Arizona*
[d]*NASA Jet Propulsion Laboratory - California Institute of Technology*
[e]*The Large Binocular Telescope Observatory, University of Arizona*
[f]*Amherst College*
[g]*Kavli Institute for Particle Astrophysics and Cosmology, Department of Physics, Stanford University*
[h]*Space sciences, Technologies and Astrophysics Research (STAR) Institute, University of Liège*
[i]*PBSci-Astronomy & Astrophysics Department, University of California, Santa Cruz*
[j]*Minnesota Institute for Astrophysics, University of Minnesota*

The jovian moon Io hosts the most powerful persistently-active volcano in the Solar System, Loki Patera,[1,2] which is composed of a 21,500-km^2 warm patera floor[3] surrounding a mostly-cool central "island".[4] The temperature gradient seen across areas of the patera indicates a systematic resurfacing process,[4,5,6,7,8,9] which has been seen to occur typically every one to three years since the 1980's.[5,10] Analysis of past data has indicated that the resurfacing progressed around the patera in a counter-clockwise direction at a rate of 1-2 km/day, and that it is caused either by episodic eruptions that emplace voluminous lava flows or by a cyclically-overturning lava lake contained within the patera.[5,8,9,11] However, spacecraft and telescope observations have been unable to map the emission from the entire patera floor at sufficient spatial resolution to establish the physical processes at play. Here we present temperature and lava cooling age maps of the entire patera floor at a spatial sampling of $\sim$2 km, derived from ground-based interferometric 4.8-μm imaging of thermal emission from Loki Patera obtained on UT 8 March 2015 as the limb of Europa occulted Io. Our results indicate that Loki Patera is resurfaced by two waves that propagate and converge around the central island. The different velocities and start times of the waves indicate a non-uniformity in the lava gas content and/or crust bulk density across the patera. Future applications of this technique can yield information on the time-evolution of Loki Patera and provide insight into how Io's volcanism operates in this extreme environment.

We observed Io with the Large Binocular Telescope (LBT) during a mutual occultation event in which Europa passed in front of Io (Figure 1). During the event, images were obtained with the LMIRcam camera at a wavelength of 4.8 μm, using the LBT Interferometer (LBTI) and adaptive optics.[12,13,14] The sampling cadence of 120 ms corresponds to a 2-km advance of Europa's limb across Loki Patera between successive exposures. Although satellite occultations have been used for decades to study Io,[15] advanced adaptive optics technology and dual-telescope interferometric imaging provide unprecedented sensitivity for individual, identifiable hot spots on Io, permitting high cadence sampling and thus high spatial resolution mapping. From the images, we extract a high-time-resolution occultation light curve (Figure 2) which we use to derive temperature and lava age maps of Loki Patera (Figure 3; see Methods). Although the calibrated 1σ uncertainty in the total flux density corresponds to only 1 K in temperature, many factors influence the conversion of flux density to temperature, including assumptions about the pixel filling factor and lava emissivity. Noise in the light curve, which is correlated on sub-second timescales, also introduces some uncertainty into the reconstructions. As discussed in Methods, the maps shown in Figure 3 are optimized to match the observations without over-fitting these artifacts. In addition, the temperature distribution at small (~few km) spatial scales cannot be uniquely recovered, and structure in the maps at these scales can be viewed as a representative model that provides a good fit to the data and is consistent with the robust large-scale gradient.

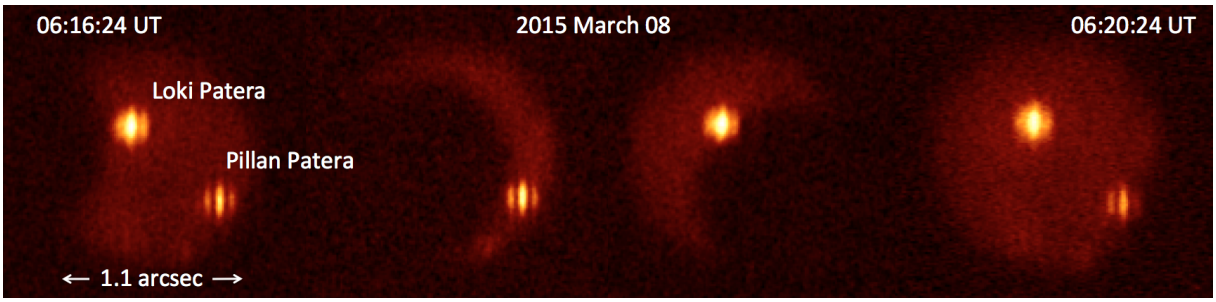

Figure 1: Observations of Europa occulting Io. Four of the ~3000 4.8-μm images obtained on UT 8 March 2015 with LBTI as Europa occulted Io. Water ice on Europa's surface absorbs incident sunlight, while Io's surface is more reflective at this wavelength. The thermal emission from Loki Patera and Pillan Patera stand out prominently against Io's disk. The fringe pattern of their emission is a product of interferometric imaging, which combines light from the two LBT telescopes.

Existing models for cooling silicate lavas[1] relate the temperature map to a solidified lava age map (Figure 3). The age map reveals the presence of two resurfacing waves: one starting in the northwest corner (Location 1 in Figure 3) ~250 days prior to the date of our observations and moving at a rate of 1 km/day in the clockwise direction, and a second wave starting in the west (Location 2) ~180 days prior to our observations and proceeding at 2 km/day in the counter-clockwise direction (see Figure 4). These rates reflect the average intensity gradient across each region of the patera; the resurfacing rate may also vary locally. The waves converged in the southeast of the patera (Location 3) and began to solidify ~75 days prior to our observations. The specific distribution of lava ages across the patera encodes information about the resurfacing process.

The temperature and age maps show that the resurfacing mechanism within the patera is considerably more complex than previously modeled. The presence of a large-scale temperature gradient indicates a coherent process acting across the entire 200-km-wide feature. High-resolution *Galileo* observations imaged a smooth temperature gradient across part of the patera.[4,6,7,9] Although the occultation technique cannot recover temperature structure at the small spatial scales probed by *Galileo*, the LBT data reveal that this is not a local effect; the presence of a temperature gradient that is coherent across large areas of the patera is a fundamental feature of the resurfacing process of the entire Loki Patera.

Time-series data from Keck and Gemini N indicate that Loki Patera's episodic activity had been ongoing since at least 2013.[17] The LBT observations were obtained 6-8 months after the start of the preceding

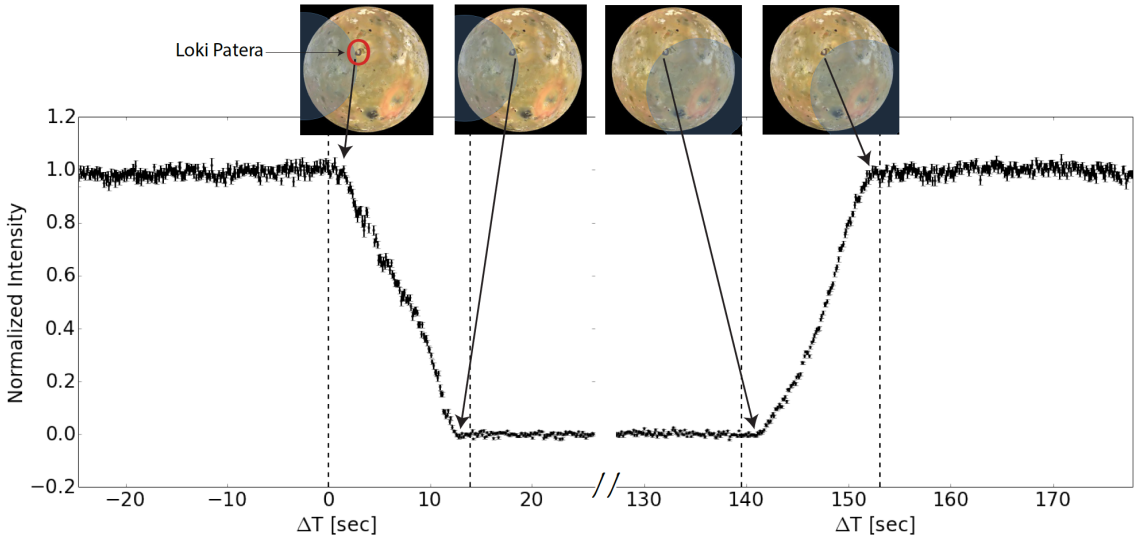

Figure 2: Occultation light curve. The occultation light curve normalized to the out-of-occultation intensity of Loki Patera (see Methods). The four panels at the top of the figure indicate the position of Europa (shown as a circular shadow) relative to Loki Patera at different times during the occultation. The vertical dashed lines separate the occultation datapoints that are used in the modeling from the baseline data. The pre-ingress and post-egress points are used to determine the baseline noise distribution. The time T=0 seconds represents the start of the occultation data used in the modeling.

brightening event (Jul/Aug 2014), and 2-3 months after its conclusion (Dec 2014).[17] The lava age map demonstrates that the majority of the patera floor is younger than 200 days, which matches the date this brightening began and confirms that the entire patera was resurfaced during the most recent event. In addition, the age of the youngest lava surface (∼75 days old) is consistent with the end date of the most recent brightening episode, demonstrating that no localized activity has taken place since the end of the last event.

The two resurfacing waves began in the west margin at different dates (ΔT=50-100 days) and moved around the central island until they converged in the southeast corner (Figures 3 & 4). Although the data do not allow a definitive identification of the resurfacing mechanism, the presence of a "double-wave" has implications for both the foundering lava lake crust and the lava flow models.

If Loki Patera is being resurfaced by lava flows, the episodic magma supply must consist of two steady pulses of magma reaching the surface at nearby yet distinct times and locations. The difference in areal resurfacing rate between the northern and southern parts of the patera also requires differences in magma properties or discharge rates between these locations. Although different flow rates could also be caused by local topography, the flatness of the patera floor as seen by *Galileo*[18] disfavors this explanation. The resurfacing rate for the southern part of the patera is twice the rate observed in 2001 *Galileo* NIMS data in the same part of the patera (∼1 km/day[8,9]), suggesting that the differences are due to variable lava properties rather than fixed localized effects.

In the lava lake foundering crust scenario,[5,9,19] the resurfacing rate is diagnostic of the bulk density structure of the crust. The presence of two resurfacing waves moving at different rates implies independent sources of magma along the western edge of the lake, with a higher bulk density in the southern magma source to explain the faster resurfacing. This density difference indicates either a difference in magma composition or, more likely, a difference in the amount of gas in the magma, which forms voids in the crust as it solidifies and decreases the crust bulk density.[5,19] A higher crust bulk density causes the crust to sink sooner after solidification, while a lower lava porosity slows the cooling of the crust, decreasing the rate of progression of the foundering wave.

The presence of the cool "island" in the middle of Loki Patera (Figure 3) is required to fit the data

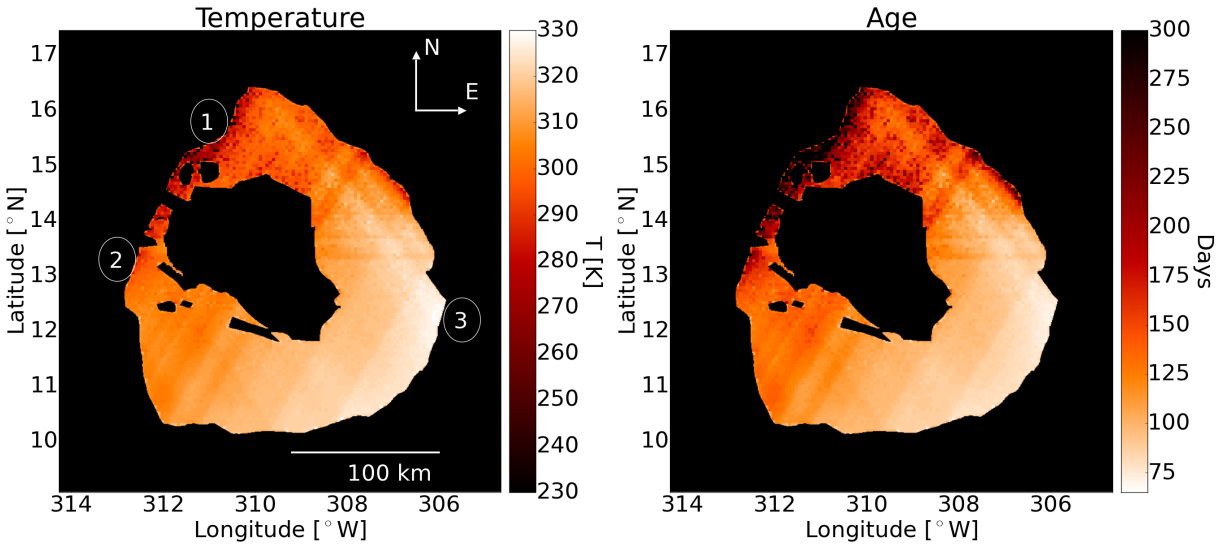

Figure 3: Temperature and age maps of Loki Patera. The outline of the patera and the cool central island are fixed based on spacecraft imaging data,[16] and the intensity distribution is determined by fitting a model to the occultation light curve. Locations 1 and 2 indicate the approximate regions where the two resurfacing waves originated; both waves progressed eastward around the island and converged at Location 3. The maps assume an emissivity of 1 and a basaltic lava composition. The striping effect is an artifact produced by correlated noise in the light curve (see Methods for details).

(see Methods). We confirm that the cool island is still present, and is therefore a long-term fixture of the patera, persisting for at least the 36 years since it was first seen during the *Voyager* encounter in 1979. The island has withstood the physical and thermal stresses imposed by the eruption of thousands of km^3 of lava adjacent to it, indicating that it is an anchored feature rising up through the surrounding lava, rather than a large raft on a sea of magma.

Temperature maps of portions of the patera have been previously derived from high-resolution *Galileo* NIMS observations obtained in 1999 and 2001.[2,4,8,9] Although the intrinsic variability of Loki Patera limits the value of direct comparison between observations obtained years apart, the propagation rate of the resurfacing wave derived from our age maps is consistent with the 1-2 km/day rates derived from both these NIMS data and *Galileo* PPR observations,[5,6,7] as well as earlier *Voyager* data.[5] In addition, the counter-clockwise progression of the wave in the southern part of the patera matches the direction derived from the *Voyager* and *Galileo* observations.[5,8,9] These results were seemingly contradicted by time-series adaptive optics data from the Keck and Gemini N telescopes,[17] which suggest a clockwise resurfacing direction. The discovery of two resurfacing waves, one of which moves clockwise in the north, and the other counter-clockwise in the south, can reconcile these apparently contradictory results. Although the details of the resurfacing may vary between each brightening cycle, all past observations of Loki Patera are consistent with the overturn progression described herein, in combination with sporadic activity at the southwest margin.

Acknowledgement

The Large Binocular Telescope is an international collaboration among institutions in the United States, Italy and Germany. The LBT Corporation partners are: The University of Arizona on behalf of the Arizona university system; Istituto Nazionale di Astrofisica, Italy; LBT Beteiligungsgesellschaft, Germany, representing the Max-Planck Society, the Astrophysical Institute Potsdam, and Heidelberg University; The Ohio State University, and The Research Corporation, on behalf of The University of Notre Dame, University of Minnesota and University of Virginia. The LBT Interferometer is funded by the National Aeronautics and

Space Administration as part of its Exoplanet Exploration program. The LMIRcam instrument is funded by the National Science Foundation through grant NSF AST-0705296. KdK and IdP are partially supported by the National Science Foundation grant AST-1313485 to UC Berkeley and by the National Science Foundation Graduate Research Fellowship to KdK under Grant DGE-1106400.

Author Contributions

AC, AS, DD, JL, MS, PH, CV, and CW developed and operated the instrumentation used to obtain these observations. AC, AS, AV, DD, ES, KdK, PH, and VB took the data. AR, JL, and MS performed the data reduction and calibration. KdK and MS analyzed the data. AGD, IdP, JL, KdK, and MS wrote the article and Methods section.

Materials and Correspondence

Correspondence and material requests should be addressed to Katherine de Kleer at kdekleer@berkeley.edu.

References

[1] Davies, A. *Volcanism on Io: A Comparison with Earth*. Cambridge University Press, (2007).

[2] Lopes, R. and Spencer, J., editors. *Io after Galileo*. Springer-Praxis Publishing, (2007).

[3] Veeder, G., Davies, A., Wlliams, D., et al. Io: Heat flow from dark paterae. *Icarus* **212**, 236–261 (2011).

[4] Lopes-Gautier, R., Douté, S., Smythe, W. D., et al. A close-up look at Io from Galileo's Near-Infrared Mapping Spectrometer. *Science* **288**, 1201–1204 (2000).

[5] Rathbun, J., Spencer, J., Davies, A., Howell, R., and Wilson, L. Loki, Io: A periodic volcano. *Geophysical Research Letters* **29**(1443), 1–4 (2002).

[6] Spencer, J., Rathbun, J., Travis, L., et al. Io's thermal emission from the Galileo Photopolarimeter-Radiometer. *Science* **288**, 1198–1201 (2000).

[7] Rathbun, J., Spencer, J., Tamppari, L., et al. Mapping of Io's thermal radiation by the Galileo Photopolarimeter-Radiometer (PPR) instrument. *Icarus* **169**, 127–139 (2004).

[8] Howell, R. and Lopes, R. The nature of volcanic activity at Loki: Insights from Galileo NIMS and PPR data. *Icarus* **186**, 448–461 (2007).

[9] Davies, A. Temperature, age and crust thickness distributions of Loki Patera on Io from Galileo NIMS data: Implications for resurfacing mechanism. *Geophysical Research Letters* **30**(2133), 1–4 (2003).

[10] Veeder, G., Matson, D., Johnson, T., Blaney, D., and Goguen, J. Io's heat flow from infrared radiometry: 1983-1993. *Journal of Geophysical Research* **99**, 17095–17162 (1994).

[11] Howell, R. Thermal emission from lava flows on Io. *Icarus* **127**, 394–407 (1997).

[12] Esposito, S., Riccardi, A., Pinna, E., et al. Large Binocular Telescope Adaptive Optics system: New achievements and perspectives in adaptive optics. *Proceedings of SPIE* **02**(8149) (2011).

[13] Hinz, P., Arbo, P., Bailey, V., et al. First AO-corrected interferometry with LBTI: Steps towards routine coherent imaging observations. *Proceedings of SPIE* **8445**(0U) (2012).

[14] Leisening, J., Skrutskie, M., Hinz, P., et al. On-sky operations and performance of LMIRcam at the Large Binocular Telescope. *Proceedings of SPIE* **8446**(4F) (2012).

[15] Spencer, J., Clark, B., Toomey, D., Woodney, L., and Sinton, W. Io hot spots in 1991: Results from Europa occultation photometry and infrared imaging. *Icarus* **107**, 195–208 (1994).

[16] Veeder, G., Davies, A., Matson, D., et al. Io: Volcanic thermal sources and global heat flow. *Icarus* **219**, 701–722 (2012).

[17] de Kleer, K. and de Pater, I. Io's Loki Patera: Modeling of three brightening events in 2013-2016. *Icarus* **in review** (2016).

[18] Turtle, E., Keszthelyi, L., McEwen, A., et al. The final Galileo SSI observations of Io: Orbits G28-O33. *Icarus* **169**, 3–28 (2004).

[19] Matson, D., Davies, A., Veeder, G., et al. Io: Loki Patera as a magma sea. *Journal of Geophysical Research* **111**(E09002), 1–21 (2006).

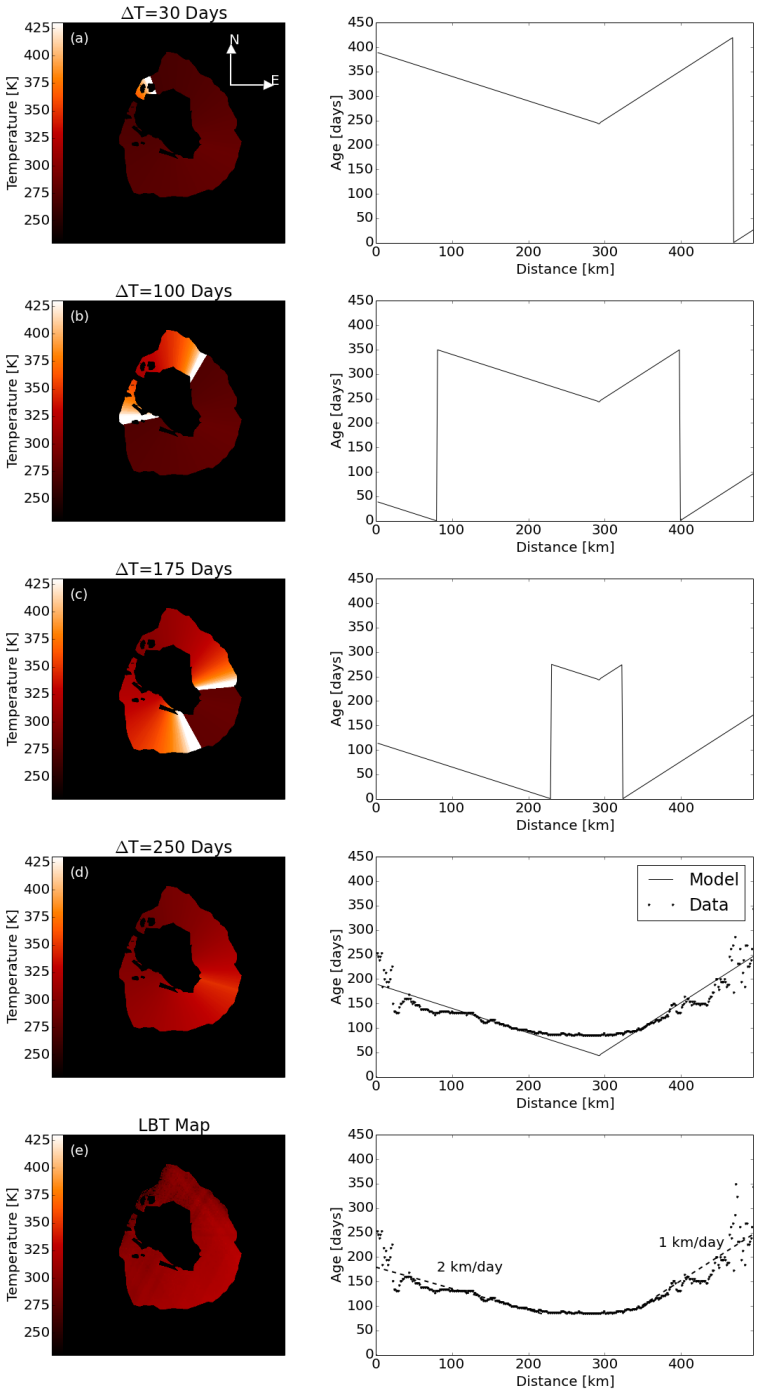

Figure 4: Overturn schematic. The sequence of images (a-d) shows model temperature maps for different stages of the dual-wave progression, assuming the idealized case of smooth, continuous resurfacing. ΔT is the time since the resurfacing initiated, and the base temperature map at ΔT=0 is the model temperature 450 days after the previous resurfacing. The plots (right column) show the corresponding patera surface age as a function of distance counter-clockwise around the patera from the narrow, northwest corner. The last row (e) shows the corresponding properties retrieved from the data. The slope of the age profile indicates resurfacing rates of 1 and 2 km/day for the northern and southern parts of the patera respectively, beginning $\sim$250 and $\sim$180 days before the date of our observations. See Extended Data Figure 6 for details on the derivation of the age profiles.

Methods

Observations: We observed the occultation of Io by Europa on UT March 8, 2015 using Fizeau interferometric imaging with the Large Binocular Telescope Interferometer (LBTI)[23,13] and the LMIRcam near-infrared instrument[14,24], which has a platescale of 0.0107"/pixel[25] (see Figure 1). Both telescopes were adaptive-optics corrected using Io as a natural guide star at R-Band for wavefront correction. During the occultation event, Europa entered the wavefront sensors' fields of view and contributed to the AO correction. Observations were acquired at M-Band (4.6-5.0 μm), which is ideally suited to image the thermal emission from volcanic structures on the surface of Io. Europa's occultation of Loki Patera began at 6:16:23 UT and completed about 150 seconds later. Integration times were set to 15.4 msec per exposure, with an average of 120 msec between each exposure start. Data were acquired in sub-frame mode (512×512 pixels) to decrease camera overheads and maximize the imaging cadence. The details of the observations are given in Extended Data Table 1.

Fizeau observations with LBTI coherently combine the light from the LBT's two AO-corrected[12] 8.4-meter mirrors to produce a characteristic interference pattern along the direction of the two-telescope baseline.[13] These types of observations result in an increased spatial resolution across the diffraction fringes while also concentrating more of the light into the central core of the point spread function (PSF).

For this sequence of observations, and all Io observations with LBTI, the fringe sensor cannot operate because Io is completely resolved and Loki Patera is too faint in the near-infrared to serve as a point source for automated phase stabilization. The interference pattern therefore drifts around a central (white-light) fringe due to small changes in the path-length difference between the two telescopes caused by instrumental vibrations and atmospheric disturbance. Throughout the observations, phase stabilization was performed manually through tracking of the M-band fringes.[20]

Although the LBT's Fizeau mode of operation delivers the ultimate diffraction-limited performance of the 22.8-meter effective diameter of the LBT, that resolution (30 milliarcsecond diffraction limit at 4.8 μm) only corresponds to a 100-km spatial resolution at Io[20], much lower than the 2 km frame to frame limb motion of Europa in the time-resolved occultation profiles. The primary advantage of the use of adaptive optics and Fizeau interferometry for the observation reported here is in resolving the individual volcanic sources on Io's ∼1.0" diameter disk and maximizing the signal-to-noise ratio for each source by minimizing the angular size of the PSF and thus the local thermal background contributing to the noise.

Europa's gradual occultation of Io's surface systematically blocks flux from volcanic hot spots at each time step, providing spatial information along the direction of motion of Europa's edge. With a limb motion of ∼5.5 milliarcseconds/sec (20 km/sec) relative to Io's disk, the 120 msec observing cadence corresponds to a spatial sampling resolution of 2.4 km. Due to the noise on individual datapoints, the effective spatial resolution is a factor of a few lower than this.

Mutual occultation events between the galilean satellites occur for periods of several months every six years. During each such period, there can be over a hundred occultations of Io by one of the other satellites. While not all are optimal for the LBTI techniques discussed here, nor observable from a given terrestrial hemisphere, the quantity of such events provides many opportunities for performing similar observations in the future. The experimental approach is also applicable to observations made with high-Strehl adaptive optic systems on any large (8-10-m class) near-infrared telescope, provided the AO system and camera are suitable.

Data reduction: Standard LMIRcam image reduction was performed, which consists of linearity correction, sky background subtraction, reference pixel correction, bad pixel removal, and distortion correction. Flat-fielding was not performed because the pixel response is intrinsically flat across LMIRcam's entire detector and the region of interest is small (1"×1") compared to the instrument's full field of view (20"×20"). The final reduced images show excellent uniformity (<1% deviation) across the observed field. A series of background observations were acquired before and after the occultation with Io nodded to a separate detec-

tor position. For each Io science frame, the 500 background frames closest in time were median-combined and subtracted from the science frame. The removal of sky background also removes the detector bias and any dark current contributions.

Background removal: Individual images from the occultation event show Io as a bright disk covered with volcanic hot spots being occulted by a dark Europa (see Figure 1). Reflected sunlight makes the disk of Io visible, while strong water ice absorption causes Europa to reflect much less sunlight than Io. Precise aperture photometry of Io's volcanoes requires a uniform background and thus modeling and removal of the "crescent" of the bright disk of Io. Gaussian convolution of a multi-parameter model with the telescope point spread function produces synthetic, volcano-free images for frame-by-frame subtraction from the data. The model parameters include the disk flux, the radii of Io and Europa, the angular offset between the centers of the bodies, and limb darkening. The final synthetic image is produced by optimizing these model parameters via a gradient descent algorithm. Prior to aperture photometry, the model is directly subtracted from the background-corrected data on a frame by frame basis, yielding a sequence of images of the hot spots alone. An example image is shown in Extended Data Figure 1 before and after this correction is applied.

Frame registration and alignment: The background-subtracted images are rotated to position Io's polar axis in the horizonal direction. The relative positions of both Loki Patera and Pillan Patera are then tracked frame-to-frame using a combination of gaussian centering and cross-correlation with respect to a median-combined reference PSF. Monitoring of Pillan Patera's position provides an extra check on the location of Loki Patera, particularly during Europa's ingress. This method enables sub-pixel frame registration.

Light curve extraction: Aperture photometry provides the flux measurements contributing to the observed light curve (Figure 2). A circular aperture with a 13-pixel ($\sim$140 mas) radius optimized the signal-to-noise ratio, and was used for the photometry. This corresponds to the approximate full width at half maximum of a single-aperture point spread function (1.2λ/D). Due to the lack of closed-loop phase stabilization, the fringed PSF oscillates around a central fringe, but generally stays contained within a region corresponding to the central core of a single-aperture Airy pattern.[14] An aperture size similar to that of the central core (especially after frame registration) therefore collects the vast majority of the source flux even if the phasing is imperfectly aligned. The 13-pixel aperture radius corresponds to a full aperture width of $\sim$1000 km on Io's surface, or five times the physical width of Loki Patera. The images shown in Figure 1 demonstrate that Loki Patera is the only bright hot spot located within the extraction aperture. If small nearby hot spots were present within the aperture but indistinguishable from Loki Patera in the images, the occultation of these hot spots would be present in the light curve of Loki Patera at a time offset from that of the main ingress and egress. Since no additional dip in intensity is seen in the light curve (see Figure 2), the presence of other hot spots within the extraction aperture with flux density above the noise ($\sim$2% of Loki Patera's intensity) can be ruled out.

The flux density of the spatially-distinct Pillan Patera hot spot (see Figure 1) is simultaneously extracted to monitor any fluctuations during Europa's transit. Because changes in atmospheric transmission or AO performance would affect the flux from both volcanoes similarly, Pillan Patera could function as a baseline to correct those fluctuations in Loki Patera's light curve that would otherwise be indistinguishable from occultation effects. The baseline measurements of both Pillan Patera and Loki Patera show low-order variations of $\sim$2% over 10's of seconds, indicating good stability. We opted to exclude these corrections because of the negligible impact on the final light curve relative to the measurement uncertainties. Flux uncertainties are derived for each frame by measuring the pixel-to-pixel variations in the sky annulus. The uncertainty measurements closely match the standard deviation of baseline sections of the Loki Patera and Pillan Patera light curves.

Flux Calibration: The absolute unocculted intensity of Loki Patera is derived by calibrating to the standard star HD 81192, which was observed 1.5 hours after the occultation of Loki Patera. The reference star observations were performed in similar conditions as the Io observations (1.1 airmasses, 1" seeing, and 6 mm of precipitable water vapor). We assume that atmospheric transparency and AO performance stayed

constant based on the consistent, stable weather conditions and the fact that observations of both Io and HD 81192 showed very little variations in the measured counts. For a given extraction aperture, the total counts for Loki Patera were measured relative to that of HD 81192. We used a variety of aperture sizes in order to determine if the extended nature of Loki Patera produced any significant flux loss. Count ratios were consistent for apertures radii greater than 10 pixels, and gave an intensity ratio of 3.660 ± 0.035 between HD 81192 and Loki Patera. Utilizing the Python code Pysynphot[26], a Phoenix model template for a G7III type star was normalized to the 2MASS and WISE measurements of HD 81192. The throughput curve of LMIRcam's M-Band filter transmission was then convolved with the normalized template to determine the apparent magnitude of HD 81192 as seen at M-Band. We calculate the total flux density of Loki Patera to be 0.950 ± 0.025 Jy. The uncertainties include propagated errors from the flux ratios, normalization uncertainties based on the 2MASS and WISE error bars, and possible mismatches to the spectral template.

Light curve modeling: The change in the integrated brightness of Loki Patera at each timestep during ingress and egress represents the amount of emission coming from the strip of the patera that is covered or un-covered during that time interval. The occultation light curve can therefore be used to re-construct the distribution of emission from the patera floor. The difference in orientation between the directions of motion of Europa's limb across Loki Patera during ingress and egress permits a reconstruction of the full two-dimensional thermal emission map. We reconstruct this map by creating model emission maps, generating the model light curves, and fitting these light curves to the observations. The direct product of the modeling process is a map of the 4.8-μm intensity within the patera; this is converted to a temperature and lava age map as described later in the text. Retrievals using models that span a wide range of parameters, resolutions, and fitting algorithms all recover the same qualitative features in the intensity map.

Model intensity map: The base map for the intensity modeling is a patera outline derived from *Voyager* spacecraft imaging[16] (see Figure 3). The exact duration of ingress and egress yield the width of the warm patera area in the direction of motion to within a few kilometers. The widths derived for both ingress and egress match the *Voyager* shape to within uncertainties, indicating that the general size and shape of Loki Patera has not changed significantly in the past 36 years, and demonstrating that the use of this outline in the modeling does not introduce significant bias.

Within the fixed patera outline, the patera area is divided into pixels, and the value of each pixel is fit independently in the retrievals. Pixel sizes from 2 km up to 40 km are tested, and two shapes are used. Diamond pixel shapes follow the ingress and egress directions: the edges of the diamonds are parallel to Europa's limb as it crosses that portion of the patera, minimizing the number of light curve points that constrain the value of each pixel. The diamond shape is useful for comparing between the light curve and the intensity distribution, and in particular for identifying artifacts that are caused by small numbers of anomalous points in the light curve. However, the final maps presented here make use of square pixels, where the value of each pixel is constrained by a larger number of timesteps. The pixel size determines the number of independently-fit intensity units within the patera. However, the model treats partial pixel coverage by Europa's limb with an accuracy down to sub-km scales. The maps shown in Figure 3 use square pixels sized 2 km$\times$2 km.

Model light curve: Ephemeris information from the JPL Horizons database is used to determine the position of Europa's limb relative to Loki Patera. The time resolution of the available ephemerides is lower than the observing cadence, and the ephemeris values are therefore linearly interpolated to each observation time based on the bracketing timesteps. At each timestep, the relative positions of Io and Europa are read from the ephemeris; the location of each point within Loki Patera is calculated relative to Io's center; and the resultant distance from Europa's center to each point within Loki Patera is compared to Europa's radius to determine if that point is obscured. The total intensity in the unobscured portion of the patera corresponds to the simulated light curve value at that timestep. By using ephemeris information for each timestep, the movement of both Io and Europa are accounted for, as is Io's rotation over the course of the event. Extended Data Figure 2 demonstrates model light curves for simple models with uniform intensity distributions within

the patera.

Fitting methods: The model light curves are fit to the observations by allowing all pixels in the model intensity map to vary as free parameters in the fit. Multiple fitting algorithms were tested, including Markov Chain Monte Carlo (MCMC) simulation[27], bounded limited-memory Broyden-Fletcher-Goldfarb-Shanno (BFGS) optimization[28], and the Truncated Newtonian algorithm (TNC)[29]. All fitting methods produce similar qualitative results. The TNC algorithm is chosen for the fits presented here because it is significantly faster than MCMC and produces less artifacts in the intensity maps than the limited-memory BFGS optimization.

Model selection: The presence of correlated noise in the light curve (Figure 2) requires a careful analysis of goodness-of-fit metrics to avoid over-fitting the data and introducing artifacts into the modeled intensity maps. The fitting algorithms rely on minimizing χ^2 to within a specified fit tolerance. However, χ^2 is not a meaningful metric for determining fit quality or comparing between models because the model complexity is not accurately represented by the number of free parameters, nor is the model complexity easy to quantify[30,31]. It is therefore not possible to determine whether a model is under-fitting or over-fitting the data by looking at χ^2 alone.

An alternative method for determining whether the model provides a good fit is the Kolmogorov-Smirnov test (KS-test) p-value[32,33]. The KS-test uses the distribution of the residuals from a given model to determine whether the residuals could have been drawn from a normal distribution, as would be the case for random noise. If the p-value is below 0.01, the hypothesis that the residuals are drawn from a normal distribution is rejected with 99% significance; a p-value greater than 0.01 indicates consistency with a normal distribution.

The standard KS-test is based on the assumption that noise in the dataset is random. However, the occultation light curve contains non-random noise, and the standard KS-test is therefore not a good assessment of model fit. Instead, the two-sample KS-test is employed, which compares the residuals to a more realistic noise distribution based on the dataset itself. Given a reference noise distribution, the two-sample KS-test evaluates whether the residuals from the light curve model fit are consistent with the reference noise level. Two reference noise distributions are considered in this analysis: the baseline noise of Loki Patera in the $\sim$10 seconds prior to ingress and the $\sim$10 seconds immediately post-egress, and the residuals on the simultaneous intensity of Pillan Patera. Because Pillan Patera was occulted during the Loki Patera egress, the latter method can only be applied to the Loki Patera ingress.

For a given pixel shape and size, the preferred model is chosen to correspond to the loosest fit whose residual distribution is consistent with the best noise distribution available. In the case of ingress, this is the simultaneous noise distribution of Pillan Patera, while on egress this is the post-egress baseline level of Loki Patera. Extended Data Figure 3 shows example fits using square 8-km pixels (lower than the resolution of the final maps) for a range of fit tolerances. The corresponding model light curves are shown in Extended Data Figure 4 and the p-values are given in Extended Data Table 2. The preferred model is the loosest fit for which the residuals are consistent with the expected noise at 99% significance (Fit C in Extended Data Figure 3). This requirement ensures that the light curve is neither under-fit nor over-fit.

In addition, the optimal fit can be identified qualitatively as the closest fit that stays consistent with the broad-strokes distribution represented by the loosest fit (Fit A in Extended Data Figure 3). As the fit constraints tighten, the big-picture distribution stays consistent but becomes more resolved. However, around Fits D-E the distribution deviates and prominent striping artifacts appear. Fits C and D demonstrate this turnaround point, where the light curve is being fit closely but artifacts are only just beginning to appear. Using this criterion, the retrieved intensity distribution on the patera floor is not highly sensitive to number of independent pixels that are fit for, nor to the shape of the pixels (see Extended Data Figure 5).

Retrieval accuracy: Our model selection is based on the assumption that the striping structure in Fits E and F is due to noise in the data, although we cannot rule out the possibility that some of this structure represents real temperature structure in the patera. The assumption that the striping is an artifact is supported

by (1) the fact that presence of real structure within the patera that coincidentally aligns exactly along the directions of Europa's limb is improbable; and (2) the comparison between square and diamond pixel maps (Extended Data Figure 5), which demonstrates that the striping effect arises primarily when the pixel shape is determined by the orientation of Europa's limb and thus constrained by the minimum number of light curve points.

In this type of reconstruction, there is some inherent non-uniqueness in the retrieved temperature structure. In particular, structure at small spatial scales cannot be uniquely recovered because the length of the limb of Europa across Loki Patera is many tens of kilometers and will homogenize variations over considerably smaller spatial scales. We test the sensitivity of the technique to discrete small-scale features in the patera using simulated intensity maps with gaussian features of different sizes and brightnesses superposed on a background patera of uniform brightness. We generate simulated light curves from the maps at the same time sampling as the data, add noise to each datapoint based on the noise in the dataset, and reconstruct the images using methods identical to those applied to the LBT data. Extended Data Figure 7 shows retrievals of simulated bright spots within the patera that constitute $\sim$5-15% of Loki Patera's total brightness and vary from 10-40 km in size (full width half maximum of the bright feature). Localized features that contribute below 5% of Loki Patera's intensity are generally undetectable. The retrievals demonstrate that the existence and location of small, bright features can be recovered in most cases. However, in the case of small ($\leq$20 km) features, the shape of the feature tends to be blurred out in the retrieved map. In addition, small bright features in certain locations produce artifacts along either of the two directions oriented with Europa's limb during the occultation (see Extended Data Figure 7d & e).

The smoothness of the temperature map shown in Figure 3 should therefore be viewed with some caution, as the retrievals tend to smooth out small, discrete features and are additionally insensitive to localized features that constitute only a few percent of the total patera intensity. However, the presence of the broad-scale temperature gradient from the northwest to the southeast of the patera is not susceptible to these ambiguities. Thus while the LBT observations do not constrain the presence of localized non-uniformities in the resurfacing, the existence of a coherent volcanic process acting across both the northern and southern patera regions is robust.

As a simple test, we apply the same methods to retrieve the temperature map shown in Figure 4 for day ΔT=250 days, which approximates the LBT map. Extended Data Figure 8a demonstrates that the smooth gradient across the northern and southern parts of the patera is retrieved well. For comparison, we perform the same analysis on a simulated temperature map whose azimuthally-smoothed intensity profile is comparable to that of the LBT map, but which models the temperature gradient as a series of discrete bright features. As demonstrated in Extended Data Figure 8b, the discreteness of the underlying temperature map is evident in the reconstruction, despite the similarities between the model light curves (shown in Extended Data Figure 9).

Temperature map: The 4.8-μm intensity map derived by fitting the occultation light curve is converted to a brightness temperature map via the Planck function, which gives the spectral radiance as a function of wavelength and temperature. An emissivity value of $\epsilon = 1$ is used for this conversion, and it is assumed that the emission fills each pixel. The geometric foreshortening as a function of location within the patera is corrected for, but the change in the foreshortening during the occultation event is below 1% and is not corrected. The uncertainty in the flux calibration corresponds to an uncertainty in temperature on each pixel. However, the spectral radiance is very sensitive to small changes in temperature, and the flux calibration uncertainty leads to an uncertainty of only $\pm$1 K on the temperature map, well below the level of uncertainty resulting from systematic noise in the light curve.

Age map: The brightness temperature distribution within the patera is shown in Figure 3 alongside the lava age distribution based on a model which assumes a cooling lava crust on top of a basaltic lava lake.[19,21] Newly exposed silicate lava cools predictably, allowing a derived surface temperature to be mapped to a time since emplacement.[22,19] Once lava thermophysical values are selected (we use values for basalt[1,21]),

the model balances surface radiant heat loss with the conduction of heat through a thickening crust, including liberated latent heat as lava solidifies onto the base of the crust. Heat loss is buffered by the release of latent heat until the lava flow is completely solidified, after which the surface temperature falls off rapidly.[21] A lava lake is treated as a semi-infinite body, so latent heat release is always present. The lava lake and lava flow surface cooling models diverge once the lava flow is completely solid. However, the periodic resurfacing of Loki Patera resets the lava cooling clock before complete solidification occurs, and this difference therefore cannot be used to distinguish between the two models.

Extended Data Figure 6 demonstrates the determination of resurfacing rates in the northern and southern parts of the patera, based on the derived lava age map. The uncertainty on the derived ages resulting from uncertainty in the absolute flux calibration ranges from 2 days for the warmer parts of the patera ($\sim$330 K) to 12 days for the coolest temperatures ($\sim$270 K). The exact lava cooling ages in the cooler regions should therefore be viewed with caution, although in all parts of the patera uncertainties due to time-dependent noise and an incomplete understanding of the thermal properties of the lava dominate over flux calibration effects.

In addition, if the differences in magma composition or volatile content between the northern and southern parts of the patera are significant, the corresponding cooling curves may also differ. Although this introduces some degeneracy between cooling rate and resurfacing rate, either interpretation points to a regional difference in magma composition or volatile content within the patera.

Central island: Models produced from basemaps of Loki Patera with and without a cool central island indicate that many of the large-scale features of the light curve can be reproduced by including this island (Extended Data Figure 2). The ingress light curve in particular can be matched almost perfectly just by adding the island, although matching the egress light curve requires the addition of a non-uniform intensity distribution. In addition, in a model where the island pixels are also treated as free parameters in the fits, the presence of the island is recovered. As the fit is tightened, the values of the island pixels trend toward zero, and the fits thus recover the island even in the absence of any assumptions about it. Fits with 8km x 8km pixels where the island pixels are free are shown in Extended Data Figure 10; Fit C is the preferred model based on the distribution of the light curve residuals, and recovers the location and size of the island although not the exact outline seen in *Voyager* images (see Figure 3). The cracks through the island observed by *Galileo*[4] are below our detectability threshold (constituting less than one part in ten thousand of the total emission from Loki Patera), and were not included in our models.

Code Availability: We have opted not to make the code available because the technique described is non-standard and custom routines were developed for the analysis.

Methods References

20. Conrad, A., de Kleer, K., Leisenring, J., et al. Spatially resolved M-band emission from Ios Loki Patera - Fizeau imaging at the 22.8 m LBT. *The Astronomical Journal*, **149**, 175184 (2015).
21. Davies, A.G., Matson, D., Veeder G., Johnson, T., and Blaney, D. Post-solidification cooling and the age of Ios lava flows. *Icarus* **176**, 123137 (2005).
22. Davies, A.G. Io volcanism: Thermo-physical models of silicate lava compared with observations of thermal emission. *Icarus* **124**, 45-61 (1996).
23. Hill, J.M., Green, and Slagle, J.H.. The Large Binocular Telescope. *Proceedings of SPIE*, **6267**(0Y) (2006).
24. Leisenring, J., Hinz, P., Skrutskie, M., et al. Fizeau interferometric imaging of Io volcanism with LBTI/LMIRcam. *Proceedings of SPIE* **9146**(2S) (2014).
25. Maire, A.-L., Skemer, A., Hinz, P., et al. The LEECH exoplanet imaging survey. Further constraints on the planet architecture of the HR 8799 system. *Astron. Astrophys.* 576, no. A133, 10pp. (2015).
26. Lim, P. L., Diaz, R. I., and Laidler, V. PySynphot Users Guide, Baltimore, MD: STSci (2015).
27. Foreman-Mackey, D., Hogg, D., Lang, D., et al. emcee: The MCMC Hammer. arXiv:1202.3665v4 (2013).
28. Byrd, R., Lu, P., Nocedal, J., and Schnabel, R. A limited memory algorithm for bound constrained optimization. *SIAM Journal on Scientific and Statistical Computing* **16**,1190-1208 (1995).
29. Dembo, R. and Steihaug, R. Truncated-Newtonian algorithms for large-scale unconstrained optimization. *Mathematical Programming*, **26**, 190-212 (1983).
30. Andrae, R. Error estimation in astronomy: A guide. arXiv:1009.2755 (2010a).
31. Andrae, R., Schulze-Hartung, T., and Melchior, P. Dos and don'ts of reduced chi-squared. arXiv:1012.3752 (2010b).
32. Kolmogorov, A. Sulla determinazione empirica di una legge di distribuzione. *Giornale dell' Istituto Italiano* **4**, 1-11 (1933).
33. Smirnov, N. Table for estimating the goodness of fit of empirical distributions. *Annals of Mathematical Statistics* **19**, 279-281 (1948).

Extended Data

Extended Data Table 1: Observations. Data taking during the 150-second occultation event on UT 8 March 2015. The five rows correspond to the timing regimes shown in Figure 2[a].

Phase	UT Range	ΔT [sec]	Frames	Notes
Before	06:15:23 - 06:16:22	59	480	Used for baseline noise distribution.
Ingress	06:16:22 - 06:16:36	14	110	Used in the fit.
Occulted	06:16:36 - 06:18:41	125	1020	Not used.
Egress	06:18:41 - 06:18:55	14	110	Used in the fit.
After	06:18:55 - 06:19:33	38	281	Used for baseline noise distribution.

[a] All frames were taken at M-band ($\lambda = 4.8\mu$m) with a per-frame integration time of 15.4 msec.

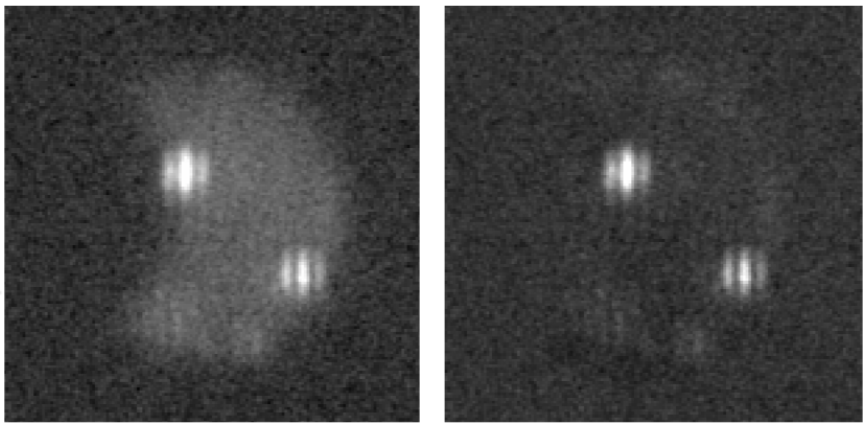

Extended Data Figure 1: Io disk subtraction. Image of Io from LBTI during the occultation. The image is shown before and after the subtraction of the reflected light from Io's disk. The residual intensity around the limb in the subtracted image is the result of imperfect limb darkening correction.

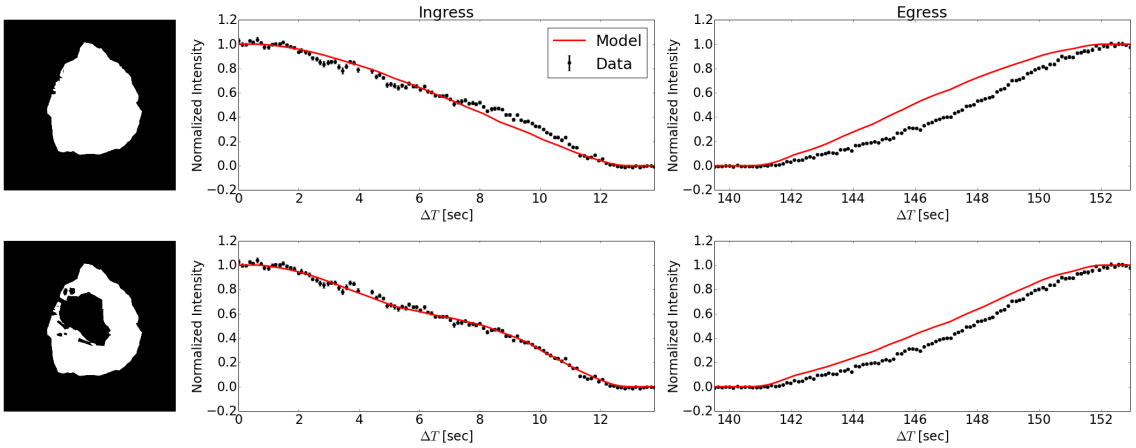

Extended Data Figure 2: Uniform-intensity models. Model light curves for models with a uniform intensity distribution within the patera, with and without a central island. The patera outline is derived from *Voyager* imaging data.[16] The model light curves in each row correspond to the image in the left panel of that row. It can be clearly seen from a comparison between the rows that the patera shape and the central island produce the broad-scale features of the ingress light curve, even without postulating a non-uniform intensity distribution. However, the addition of a non-uniform intensity distribution is required to match the egress light curve, indicating that the main temperature gradient is in the direction of motion of Europa's limb during egress (roughly northwest to southeast).

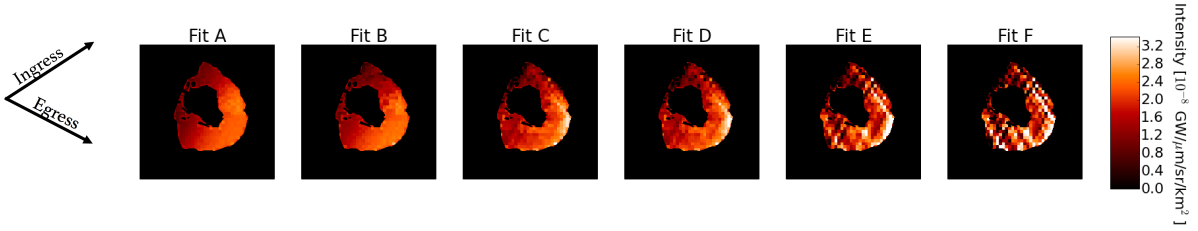

Extended Data Figure 3: Intensity maps corresponding to progressively-closer fits. Fits to the light curve using independently-fit pixels sized 8km x 8km. The series demonstrates the artifacts from systematic noise in the light curve that become increasingly prominent as the fits tighten. Fit metrics are summarized in Extended Data Table 2; Fit C is the preferred model at this resolution. The arrows at the left show the approximate direction of movement of Europa's limb during ingress and egress, demonstrating that the orientation of the limb corresponds to the striping artifacts in Fits E and F.

Extended Data Table 2: Goodness-of-fit metrics for different models.[a]

Fit	χ^2	p_{Ing}	p_{Eg}	$p_{2A,Ing}$	$p_{2B,Ing}$	$p_{2B,Eg}$
A	1178	0.0	5.11×10^{-15}	2.92×10^{-13}	7.26×10^{-18}	4.12×10^{-9}
B	741	7.56×10^{-5}	1.19×10^{-9}	0.021	1.77×10^{-3}	4.98×10^{-6}
C	534	4.31×10^{-4}	1.11×10^{-3}	0.067	0.013	0.03
D	501	9.51×10^{-3}	8.73×10^{-3}	0.24	0.047	0.11
E	399	0.043	0.034	0.4	0.18	0.38
F	360	0.043	0.091	0.24	0.34	0.5

[a] p_{Ing} and p_{Eg} are the KS-test p-values based on comparison to the normal distribution. The p_2 values are the p-values for the two-sample KS-test. $p_{2A,Ing}$ are the p-values from a test of whether the ingress residuals are drawn from the same distribution as the Pillan Patera residuals during ingress. $p_{2B,Ing}$ and $p_{2B,Eg}$ correspond to tests of the ingress residuals compared to the baseline immediately pre-ingress, and the egress residuals compared to the baseline immediately post-egress. The hypothesis that the residuals to fits A-D are drawn from a Gaussian distribution is rejected. Fit C is the loosest fit whose residuals are consistent (i.e. not excluded at the 99% level) with being drawn from the same distribution as both the nearby baseline noise and the simultaneous Pillan Patera noise, and is therefore the preferred model. All fits are to 220 data points with 250 free parameters; however, the degrees of freedom are not equal to the number of parameters, and the reduced χ^2 is therefore omitted to avoid confusion.

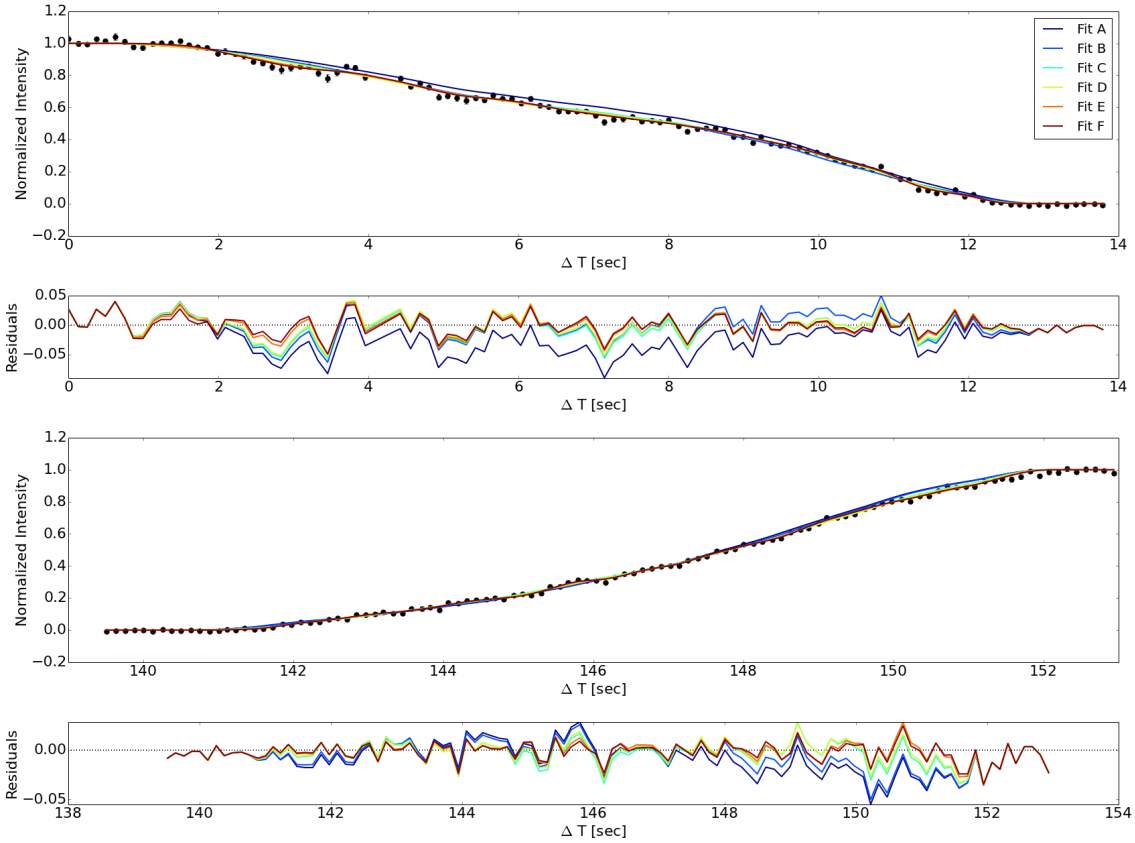

Extended Data Figure 4: Model light curves and residuals. Model light curves corresponding to the intensity maps for Fits A-F shown in Extended Data Figure 3.

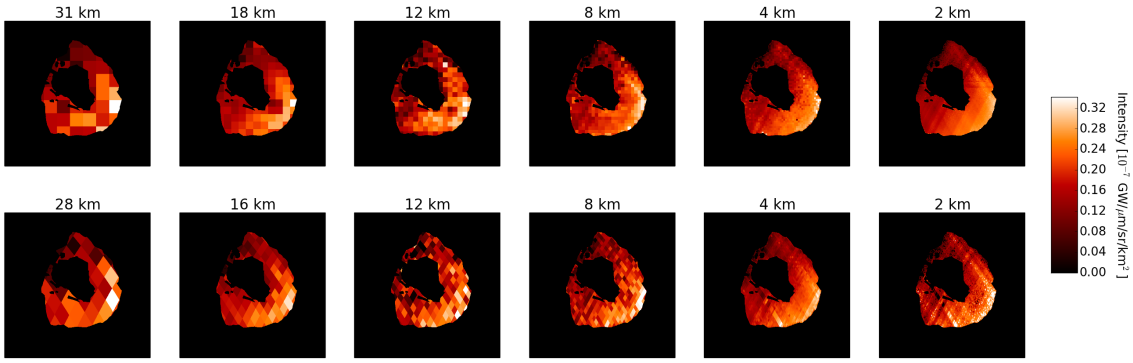

Extended Data Figure 5: Preferred models for a range of pixel sizes and two pixel shapes. The image titles indicate the size of each pixel in km. The edges of the diamond pixels are parallel to the limb of Europa as it passes that portion of the patera. Note the artifacts in the small-pixel models with diamond pixel shapes; in these models, as few as two timesteps influence the value of each pixel, and the model is thus very sensitive to noise in the light curve. These images demonstrate that the retrieved intensity distribution is consistent across different model parameters and resolutions.

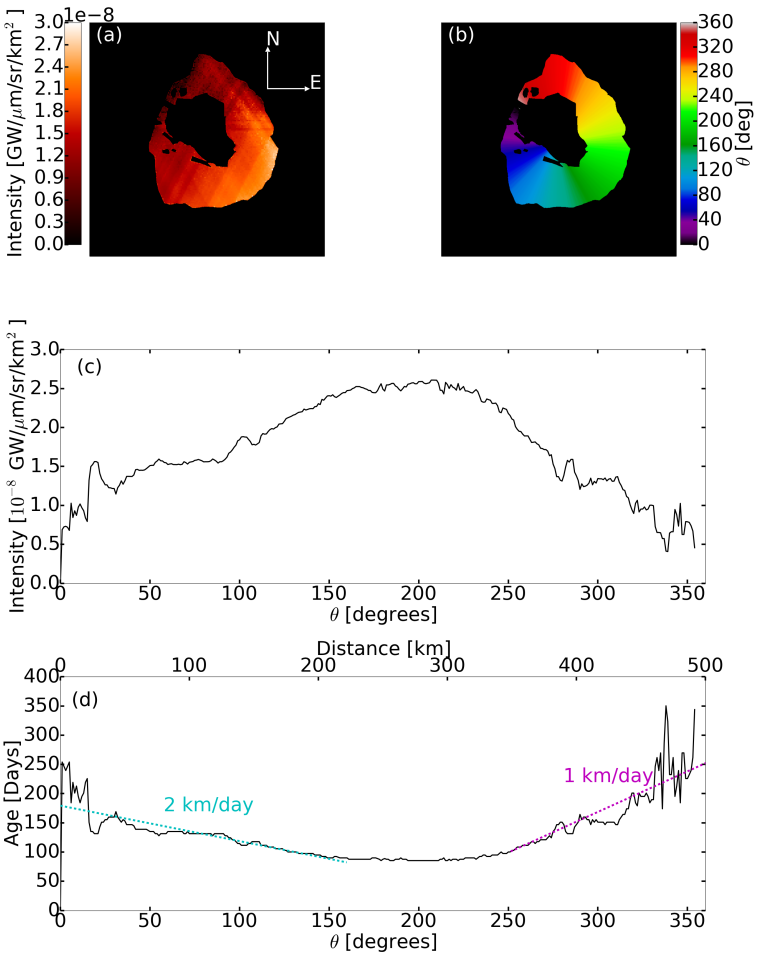

Extended Data Figure 6: Resurfacing rate. Derivation of local resurfacing rate in the northern and southern patera regions. The upper panels show the intensity map at a sampling of 2 km (panel a), and the mapping of each pixel to an angle θ that increases counter-clockwise around the patera from the west (panel b). The lower panels plot the mean intensity (panel c) and lava cooling age (panel d) as a function of the angle θ, and the approximate corresponding distance around the patera in km.

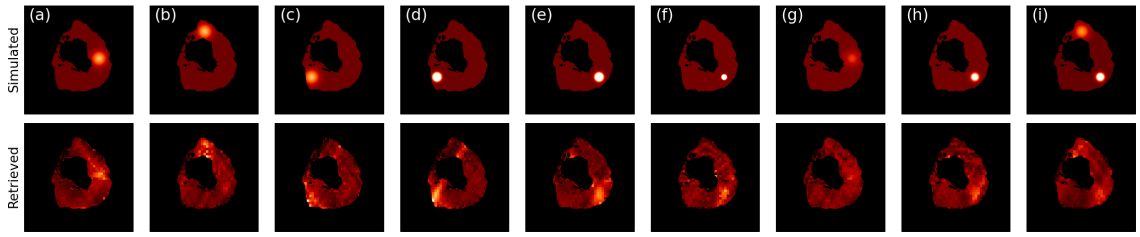

Extended Data Figure 7: Retrieval of simulated temperature maps. The simulated maps (top row) include discrete hot features of gaussian brightness distribution on top of a uniformly-bright background patera. The bright spot constitutes ∼15% of the patera's total intensity in models (a) through (e), and ∼7.5% of the intensity in models (f) through (h). The size of the bright spot ranges from 10-40 km (full width half maximum of the feature). The retrieved maps (bottom row) are generated using the same methods applied to the LBT data, based on light curves corresponding to each intensity map with realistic noise added. The figure demonstrates that the presence and location of localized hot features of these brightness levels can be accurately retrieved by the analysis methods, but not their exact shape or size.

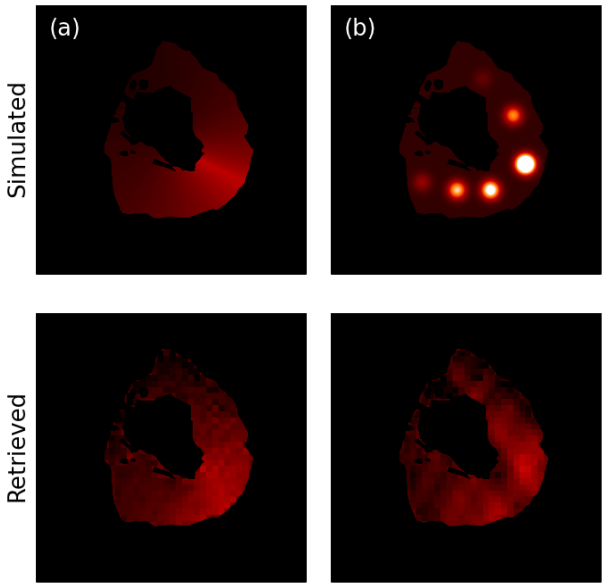

Extended Data Figure 8: Retrieval of simulated temperature maps with global gradient. The simulated maps (top row) demonstrate two possible models with similar azimuthally-smoothed intensity profiles and an overall increase in brightness toward the southeast of the patera. Simulated light curves are generated from these maps (see Extended Data Figure 9), and the maps are retrieved using the same procedure by which the LBT map is produced. The retrieved maps (bottom row) demonstrate that these scenarios are clearly distinguished by the retrieval process.

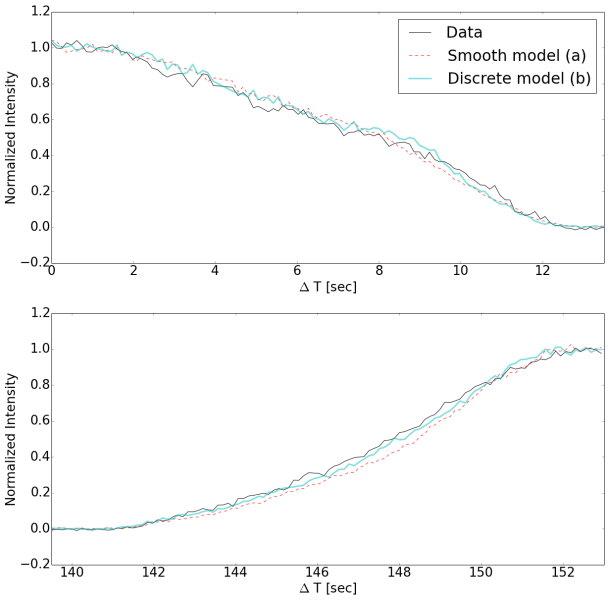

Extended Data Figure 9: Simulated light curves. The simulated light curves corresponding to models (a) and (b) from Extended Data Figure 8 are shown, with noise added, alongside the data. Although the light curves appear similar, the differences between the maps from which they are generated are clearly recovered by the retrievals.

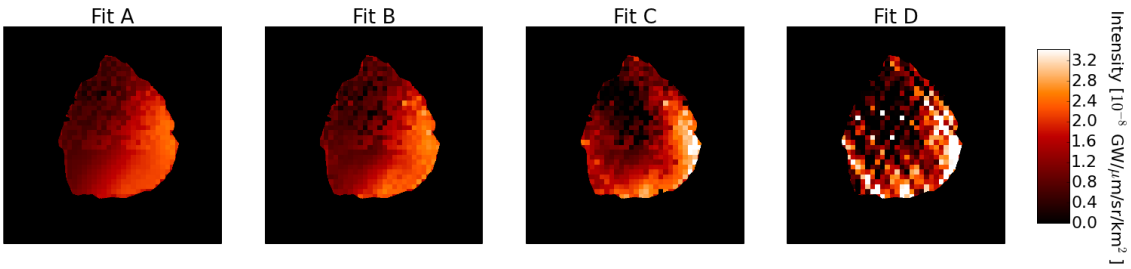

Extended Data Figure 10: Model fits without the central island. Fits using 8km x 8km square pixels, permitting the pixels in the island as free parameters in the fit. Without any assumptions about the island, the fits recover it. The preferred model based on the corresponding light curve residuals is Fit C here.